

Journal of Biomedical Optics

BiomedicalOptics.SPIEDigitalLibrary.org

Fabrication of healthy and disease-mimicking retinal phantoms with tapered foveal pits for optical coherence tomography

Gary C. F. Lee
Gennifer T. Smith
Monica Agrawal
Theodore Leng
Audrey K. Ellerbee

Fabrication of healthy and disease-mimicking retinal phantoms with tapered foveal pits for optical coherence tomography

Gary C. F. Lee,^a Gennifer T. Smith,^a Monica Agrawal,^a Theodore Leng,^b and Audrey K. Ellerbee^{a,*}

^aStanford University, Department of Electrical Engineering, Stanford, California 94305, United States

^bStanford University, School of Medicine, Byers Eye Institute, Palo Alto, California 94304, United States

Abstract. Optical coherence tomography (OCT) has become a standard tool in ophthalmology clinics for diagnosing many retinal diseases. Nonetheless, the technical and clinical communities still lack a standardized phantom that could aid in evaluating and normalizing the many protocols and systems used for diagnosis. Existing retinal phantoms are able to mimic the thickness and scattering properties of the retinal layers but are unable to model the morphology of the foveal pit, particularly the tapering of the retinal layers. This work demonstrates a new fabrication procedure that is capable of reliably and consistently replicating the shape and tapered appearance of the retinal layers near the foveal pit using a combination of spin-coating and replica molding. We characterize the effects of using different mold sizes which enable us to achieve a range of pit dimensions. We also present a modified procedure to replicate two diseased states of the retinal tissue, such as retinal detachment and dry aged-related macular degeneration. The ability to create an anatomically correct foveal pit for healthy and disease-mimicking phantoms will allow for a new standard better suited for intra- and inter-system evaluation and for improved comparison of retinal segmentation algorithms. ©2015 Society of Photo-Optical Instrumentation Engineers (SPIE) [DOI: 10.1117/1.JBO.20.8.085004]

Keywords: phantom; foveal pit; retinal diseases; optical coherence tomography; replica molding; ophthalmology.

Paper 150321PR received May 12, 2015; accepted for publication Jul. 15, 2015; published online Aug. 19, 2015.

1 Introduction

Optical coherence tomography (OCT) is a noninvasive cross-sectional imaging technique that is able to image the internal microstructures of biological tissues with high resolution in two and three dimensions; hence, it is widely used for various research and medical applications. A key application is in ophthalmology, where OCT is helpful in diagnosing retinal pathologies,¹ including macular degeneration^{2,3} and retinal detachment.⁴

To evaluate and normalize OCT system protocols, a standardized and well-characterized physical model, also known as a phantom, may be used. A standardized phantom that is reproducible and device independent can help in characterizing new OCT systems and in comparing performances across different systems.^{5,6} Synthetic phantoms also have a longer shelf life than biological samples, making them useful in the long-term characterization and evaluation of a single system over time.⁷

In the ophthalmic OCT community, a phantom that mimics the morphology of retinal tissue is particularly relevant for technical and clinical uses alike. A suitable retinal phantom should mimic the details of retinal structures with as high precision as possible.⁸ For example, the five-layered retinal phantom developed by de Kinkelder et al.⁵ was among the first to introduce differing levels of scattering for various layers, and the phantom of Baxi et al. later mimicked all 12 retinal layers.⁷ Neither phantom, however, was able to mimic the irregular, tapered structures

found near biological foveal pits. The foveal pit is located at the center of the macular of the retina and is responsible for sharp central vision. Hence, clinical imaging of the retina with OCT usually involves collecting images in the region around the foveal pit. The structural irregularity at the foveal pit (i.e., the varying thicknesses of the retinal layers due to tapering near the pit) is a key feature that frequently poses a challenge to several OCT protocols such as automated measurement of the foveal pit⁹ and layer segmentation algorithms.^{10–13} Hence, the reproduction of such irregularities in a retinal phantom is crucial to test the sensitivity and robustness of OCT systems and protocols. Rowe and Zawadzki introduced a phantom with realistic foveal pit tapering,⁸ but the materials used (glass and plastic substrates versus silicone-based materials) do not allow for accurate mimicking of scattering properties that facilitate testing of OCT protocols in the context of fuzzy boundaries as found in the eye.

Beyond challenges associated with mimicking a healthy retina, to the best of our knowledge, no retinal phantom exists that models diseased states of the retina. A phantom that includes diseased states could also help to evaluate new systems and protocols for automated diagnosis of diseases. It is known that diseases such as macular edema introduce structural irregularities that may undermine the effectiveness of some OCT protocols; for example, the layer segmentation algorithm proposed by Fernández et al.¹⁴ failed to detect all the retinal layers, largely due to the absence of a distinct foveal pit in the case of macular edema. Hence, retinal phantoms with disease-mimicking features

*Address all correspondence to: Audrey K. Ellerbee, E-mail: audrey@ee.stanford.edu

would test the rigor of computer-aided diagnosis methods, in addition to carrying the benefits of a durable and well-characterized phantom as described above.

This paper builds upon the fabrication procedure introduced by Baxi et al.⁷ for thin layer, silicone-based retinal phantoms to more accurately mimic the tapering of the retinal layers anatomically similar to biological foveal pits. In brief, we introduce a replica molding step that enables us to create patterned reliefs by spin-coating silicone layers on flat substrates. We also introduce a modified strategy to fabricate disease-mimicking phantoms that replicate the important features of two key ocular diseases, such as macular degeneration and retinal separation. A disease-mimicking retinal phantom would serve as a good standardized comparison to evaluate OCT systems and methods in distinguishing healthy and diseased retinal tissues. Generalized versions of the techniques we introduce here may also be utilized for creating other medically relevant tissue phantoms, in particular for organs that are composed of one or more thin layers and have structural irregularities (e.g., disease-mimicking skin phantoms, digestive tube, and esophageal phantoms with realistic tissue folds).

2 Features of Healthy and Diseased Retina

Let us first consider the important properties of the retinal tissue that we intend to mimic. High-quality OCT scans of healthy retinal tissue exhibit 11 distinct layers, from the nerve fiber layer (NFL) to the retinal pigment epithelium (RPE), as illustrated in Fig. 1;¹⁵ the features in the choroid layer and beyond are not typically visible under OCT. Each of the layers varies in thickness and intensity of scattering. These optical properties have been studied and reported by others.^{7,16} The foveal pit is the thinnest region, located at the macular of the retina, and is responsible for sharp central vision. In a normal retina, the foveal pit is about 150 μm in depth, 2 mm in diameter, and 6.6 deg in average slope.¹⁷ Tapering of layers around the fovea is observed in the top five layers of the retinal tissue.

OCT scans of ocular diseases have been investigated by Puliavito et al.¹ The pathologies of interest to the current

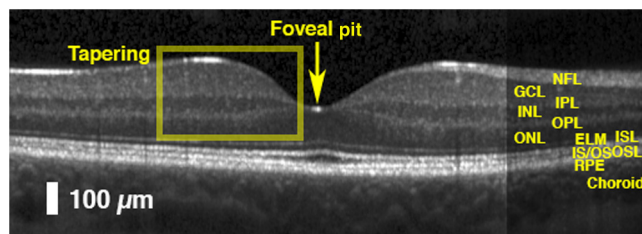


Fig. 1 Annotated optical coherence tomography (OCT) scan of a healthy retinal tissue, modified from an image by Srinivasan et al.¹⁵

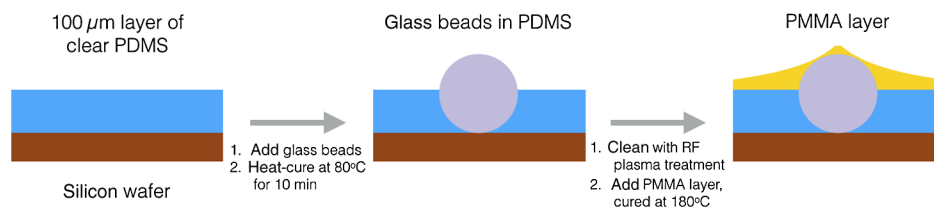


Fig. 2 Illustration of steps in the preparation of the mold using polydimethylsiloxane (PDMS), poly(methyl methacrylate) (PMMA), and glass beads.

paper include retinal detachment, which is characterized by the separation of neurosensory retina from the RPE, and age-related macular degeneration, which is characterized by drusen build-up between the RPE and the choroid.

3 Foveal Pit Mold Development and Characterization

3.1 Methods: Fabrication of the Foveal Pit Mold

Before fabricating the retinal phantom, we created a mold to induce the creation of the foveal pit. The steps are illustrated in Fig. 2. The mold is created by first spin-coating a clear polydimethylsiloxane (PDMS) layer onto a silicon wafer at a thickness of about 100 μm . Glass beads from Sigma-Aldrich [acid-washed, diameter ranges of 150 – 212 μm (Sigma G1145), 212 – 300 μm (Sigma G1277), and 425 – 600 μm (Sigma G8772)] were hand placed in the mold prior to curing at 80°C. To facilitate easy removal of subsequent PDMS layers that will make up the phantom, a thin layer (submicron thickness) of poly(methyl methacrylate) (PMMA) (MicroChem 950 PMMA C2 resist) was subsequently added and spin-coated before letting the mold cure at 180°C. It has been previously established that PDMS can be easily stripped from PMMA without tearing or the introduction of defects.^{18–20} Notably, the PDMS layer and partially submerged glass beads were plasma-treated for 2 min prior to adding the PMMA coating: the plasma treatment increases the wettability of the PDMS surface and thus facilitates irreversible sealing between it and the PMMA.²¹ Following this, layers of PDMS that are fully cured but not plasma-treated can be easily peeled away from PMMA. Since cured PDMS does not significantly modify the profile of the submerged beads, the mold can be reused several times before any significant deviation in the surface structure can be observed.

3.2 Results: Characterization of the Mold and Pit Sizes

To understand the effects of bead size on the characteristics of the fabricated foveal pit, we fabricated three different molds, each containing 10 glass beads of a single size range (i.e., protrusions) from which we created simple phantoms comprising a single layer of PDMS roughly 1–2 mm thick. The OCT scans exhibiting the cross-sectional profile of representative pits obtained from the three different bead size ranges are shown in Fig. 3. These images and all subsequent phantom images were collected with a commercial SD-OCT system (TELESTO, Thorlabs) with a center wavelength of 1325 nm. The topological profiles of the mold and the phantoms were measured by surface profilometry (Dektak 150 from Veeco), and the dimensions of

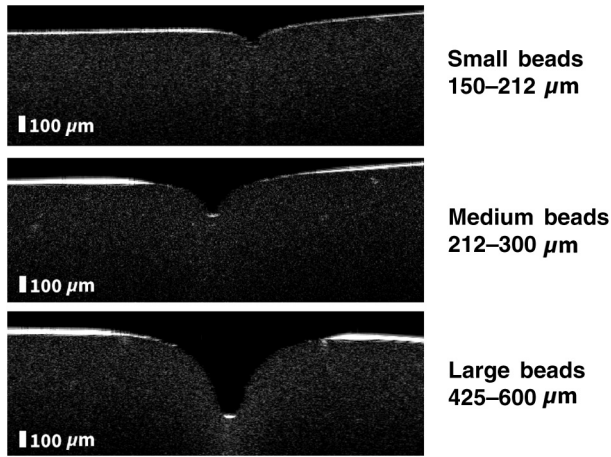


Fig. 3 OCT scans of representative pits created from each of the three bead size ranges used.

the mold protrusions and the phantom pits were subsequently extracted. The dimensions we tracked include the depth, width, and average slope of the pit created in the phantom, along with corresponding measures (height, width, and average slope) of the protrusions. We also investigated the reproducibility of the pit dimensions by repeating the above experiment to obtain a total of three trials per mold.

We define the size features of interest—the depth, width, and slope of the phantom pits and mold protrusions—as follows: the depth is taken as the shallowest point on the phantom, the width is reported as the full width at half maximum (FWHM) of the pit, and the average slope is reported as the angle derived from the arctangent of the gradient at a 1-mm distance from the pit center (note: this distance roughly matches the radius of a biological foveal pit, based on measurements from Kim et al.¹⁷). The definition of these dimensions is illustrated in Fig. 4. The measurements were extracted from one-dimensional profilometry of the phantoms and molds.

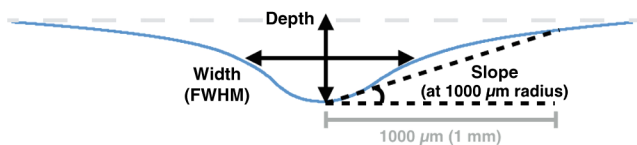


Fig. 4 Illustration of the dimensions measured on the mold and the phantoms.

Table 1 Consistency in foveal pit dimensions across three trials, demonstrated in the mean and mean absolute deviation percent (MADP) of the parameters.

Bead sizes (μm)	Depth		Width (FWHM)		Slope	
	Mean (μm)	MADP	Mean (μm)	MADP	Mean (deg)	MADP
150–212	89.8	4.20	332.4	11.97	7.75	17.84
212–250	204.0	3.43	468.9	4.66	12.68	14.09
425–600	405.5	4.99	664.9	4.71	15.95	2.44

The mean depth, width, and slope attained for each of the three bead size ranges are reported in Table 1, along with the mean absolute deviation percent (MADP) in each parameter. The MADP is calculated by taking the ratio between the average absolute deviation and the mean measurement. While the MADP for depth is generally smaller than 5% of the mean value, a larger variation among results for width and slope was observed. This may be attributed to inherent irregularities in the shape of the glass beads used. The glass beads may not be perfect spheres, resulting in pits with nonradial symmetry. As a result, any deviation in the direction of the linecut for profilometry may affect lateral measures (width and slope). Nevertheless, it is observed that the MDAP for width and slope is generally smaller with the use of larger beads.

We can precisely attain a desired pit depth by controlling the dimensions of the protrusions, as suggested by the good linear correlation between pit and mold dimensions: $R^2 = 0.9982$ for depth, $R^2 = 0.97905$ for width, and $R^2 = 0.96832$ for average slope (data not shown). Since the pits on the phantoms conform to the shape of the mold, these linear relationships were expected. Variability within the results was likely due to variability in the size and shape of the beads from a given batch and the degree to which the bead was fully embedded in the PDMS. Note that exact characterization of dimensions of the glass beads was difficult given that they were optically clear and could not be easily removed after being embedded in the PDMS.

4 Fabrication of a Healthy Retinal Phantom

4.1 Fabrication Methods

A general overview of the procedure for creating a complete phantom-mimicking healthy retinal tissue is illustrated in Fig. 5. The phantom was created in three separate parts: (1) NFL to outer plexiform layer (OPL), which include the tapering of layers at the foveal pit, (2) outer nuclear layer (ONL) to RPE, and (3) a thick choroid layer. We chose to use this procedure because it allowed us to restrict the foveal tapering to the top five layers, as tapering in biological foveal pits stops just above the ONL, while the layers ONL to RPE are thin layers and are relatively uniform. Additionally, since most pathological features are observed at the bottom layers near the RPE, separation of the phantom into different parts provides more flexibility in replicating diseased states, as will be discussed in later sections.

Similar to Baxi et al.,⁷ we implemented the layered structures in our phantom by spin-coating a silicone-based polymer mixed with scattering particles onto a silicon wafer. For our retinal phantom, we chose to use polydimethylsiloxane, or PDMS (Sylgard 184 Silicone Elastomer, Dow/Corning), mixed with varying concentrations of titanium dioxide (TiO₂) (TiO₂ anatase, 232022, Sigma-Aldrich) scattering particles with an average size of 130 ± 70 nm. To best mimic the appearance and optical properties of the retina, each layer should present with different scattering properties. We chose to utilize a single type of particle to achieve the various scattering properties (in contrast to Baxi et al., who utilized both silica microspheres and TiO₂), as matching the exact scattering properties of each layer was not our main goal. In this phantom, we neglected the effects of absorption and assumed the retina has a more dominant scattering effect; this is reasonable because the scattering coefficient in retinal tissue is significantly larger than its absorption coefficient.²² We varied the scattering in each layer by

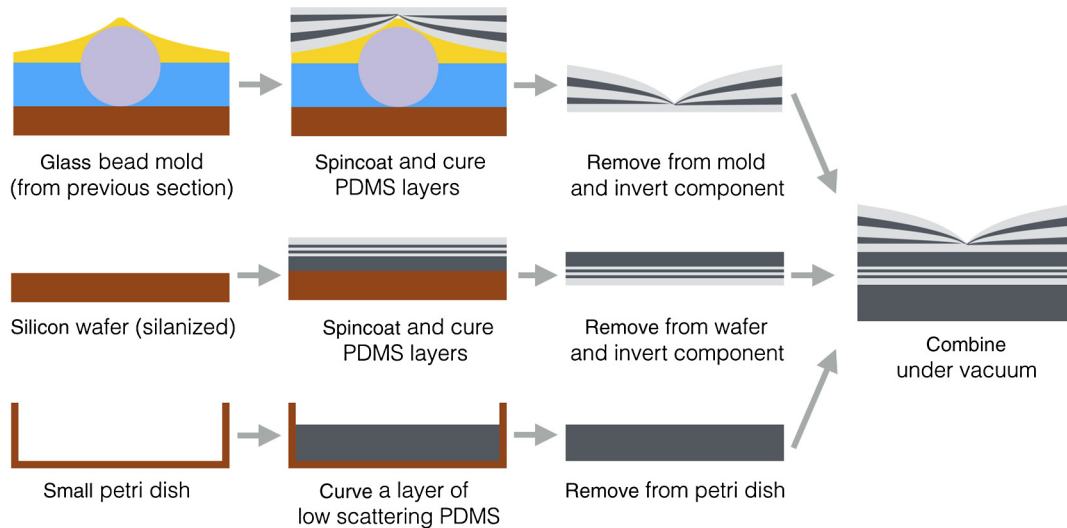


Fig. 5 Illustration of steps in fabricating the retinal phantom, which is split into three parts: (1) the top five retinal layers (NFL to OPL), (2) the next six retinal layers (ONL to RPE), and (3) the last base layer (choroid).

varying the PDMS-TiO₂ concentrations. These concentrations were determined based on the characterization performed by Greening et al.²³ Each layer was added by spin-coating for 2 min; the speed of spin-coating determined the desired thickness.²⁴ The newly added PDMS layer was cured in an 80°C oven prior to adding subsequent layers. The specifications used to achieve the respective scattering and thickness properties are presented in Table 2.

The first part of the phantom, comprising layers NFL to OPL, was created in a top-down procedure (with the NFL closest to the wafer, and the other layers on top) directly on the mold previously described for the characterization studies. The presence

of the glass bead protrusion on the mold served as a surface for uncured PDMS to adhere to, hence giving rise to tapering effects upon curing. The second part (comprising layers ONL to the RPE) was also fabricated in a top-down procedure (with the ONL closest to the wafer) on a silanized silicon wafer. The third part, representing the choroid layer, was prepared by curing low-scattering PDMS, degassed under vacuum, in a small Petri dish. The three separate parts were then combined into a single phantom by overlaying them one over another and pressing against a hard surface. The combined phantom was then placed in a vacuum chamber to ensure removal of any residual air gaps between the parts. Removing the air bubbles ensures that there will be no distinct refractive index mismatch, and is a viable alternative to a direct addition of layers through spin-coating and curing.

Table 2 Settings and specifications for fabricating a phantom for healthy retina tissue.

	Retinal layer	Spin speed (RPM)	TiO ₂ in PDMS (% w/w)
First part (NFL to OPL with tapering)	NFL	2000	0.30
	GCL	850	0.025
	IPL	2000	0.20
	INL	1250	0.025
	OPL	2000	0.30
Second part (ONL to RPE)	ONL	700	0.025
	ELM	6000	0.30
	ISL	2750	0.025
	IS/OS	5000	1.5
	OSL	5000	0.025
	RPE	2000	1.5
Third part	Ch		0.025

4.2 Results

An image of the final retinal phantom is shown in Fig. 6. The use of the mold-induced tapering of the top five layers created the shape of a foveal pit that closely resembles the morphology of an actual healthy retina. Recognizing that the literature-reported value for the average depth of biological foveal pits is about 150 μm, our characterization experiments indicated that the use of 212 – 300 μm glass beads would give rise to a phantom pit that best fits the dimensions of an actual foveal pit.

In the phantom we fabricated, the foveal pit for the retinal phantom has a depth of 163 μm, FWHM of 471 μm, and

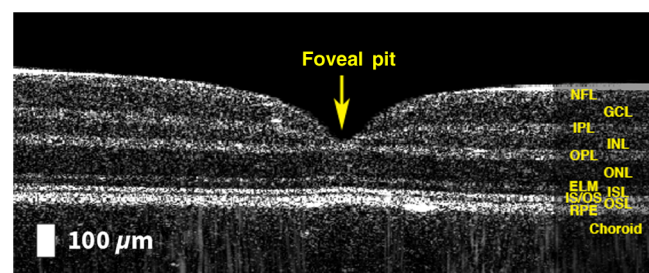


Fig. 6 OCT scan of the healthy retinal phantom.

slope of 9.46 deg. The measured depth corresponds to the reported dimensions of biological foveal pits studied by Kim et al.¹⁷ ($150.59 \pm 21.48 \mu\text{m}$). A strict comparison of the width of the phantom pit with that of an actual retinal foveal pit is difficult because the width of biological foveal pits is determined by the distance between the local maxima on either side of the pit, but this feature is absent on the phantom due to the fabrication on the flat silicon wafer. Instead, we compare the average slopes by considering that the width of biological foveal pits is about 1 mm in radius. With this definition, the average slope of the phantom foveal pit differs slightly from the biological measurement of 6.56 ± 0.56 deg. Nevertheless, the visual profile of the foveal pit in the phantom closely resembles that of biological retinal tissue. Measurements of the phantom pit could be better controlled if one has access to monodisperse beads of the desired size, which was not possible here. Furthermore, the shape of the foveal pit in the phantom is limited by the spherical geometry of glass bead protrusion and cannot be easily modified.

5 Fabrication of a Diseased Retinal Phantom

5.1 Fabrication Methods

The pathology of certain common ocular diseases of the retina, particularly the macula around the foveal pit, such as retinal detachment and dry age-related macular degeneration (dry AMD), can be replicated through modifications to the above fabrication protocols, as illustrated in Fig. 7.

Retinal detachment is characterized by a distinct separation between the RPE and the superior retinal layers. To mimic this disease, the second part of the phantom was fabricated without the RPE (i.e., layers ONL to OSL), while the third part of the phantom was fabricated to include the RPE and the choroid. We then prepared a large bump of cured clear PDMS (at least $200 \mu\text{m}$ in height) and placed it between the modified second and third parts of the phantom. After placing the completed phantom in a vacuum chamber as described above, the resulting phantom appears to have visible separation between the two layers.

Dry AMD is characterized by drusen build-up between the RPE layer and the choroid. Under OCT, the drusen appears as low-scattering protrusions located above the choroid. To replicate a single druse, we first created an epoxy inverse mold from the glass-bead mold described earlier. The choroid layer was created by curing low-scattering PDMS on the epoxy mold, giving rise to a thick choroid base with small protrusions. The modified choroid base is then firmly combined with the other two parts of the standard phantom and placed in a vacuum chamber as per the protocol described above.

5.2 Results

Figure 8 shows the OCT scans of two retinal pathologies, namely retinal detachment and dry AMD, and the corresponding retinal phantoms replicating the key characteristics of these diseases. A representative image of retinal detachment is used in Fig. 8(a) for comparison between the biological sample and our phantom. The image was acquired from a de-identified database as part of the clinical standard of care at the Stanford Byers Eye institute. The use of the image for research purposes has been approved by the Stanford University Institutional Review Board. For the dataset used, the single B-scan was centered on the fovea and consisted of 1024 A-scans with a depth of 2 mm acquired on a commercial instrument (Cirrus HD-OCT; Carl Zeiss Meditec, Inc., Dublin, California). Images were acquired at 27,000 A-scans/sec with 1024 voxels of depth over a 9-mm horizontal length. Similarly, a representative OCT image of dry AMD is used in Fig. 8(b) for comparison with our phantom and was obtained from the open dataset provided by Farsiu et al.,²⁵ which was collected using an SD-OCT imaging system from BiopTigen, Inc. (Research Triangle Park, North Carolina).

For the retinal detachment phantom, the separation of the retinal layers from the RPE is clearly replicated through the use of a cured PDMS bump which holds the separated layers in place. The size and shape of the separation may be controlled by varying the height and slope of the bump. The bump we created was at least $200 \mu\text{m}$ in height to give the appearance shown in Fig. 8(c). The position of the separation may also be changed by placing the bump at different positions relative to the foveal pit. As with typical pathologies of retinal

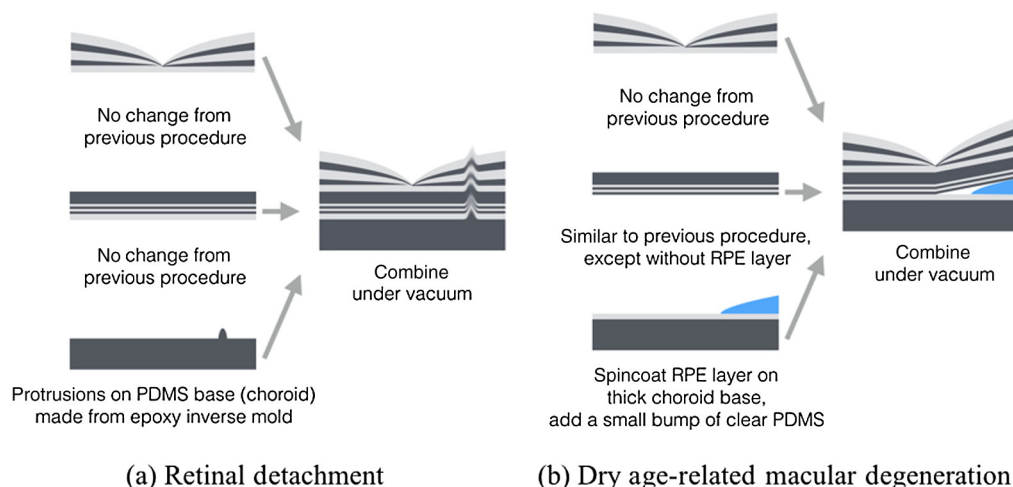


Fig. 7 Illustration of modifications introduced to induce diseased states in the retinal phantom: (a) for retinal detachment and (b) dry age-related macular degeneration (dry AMD).

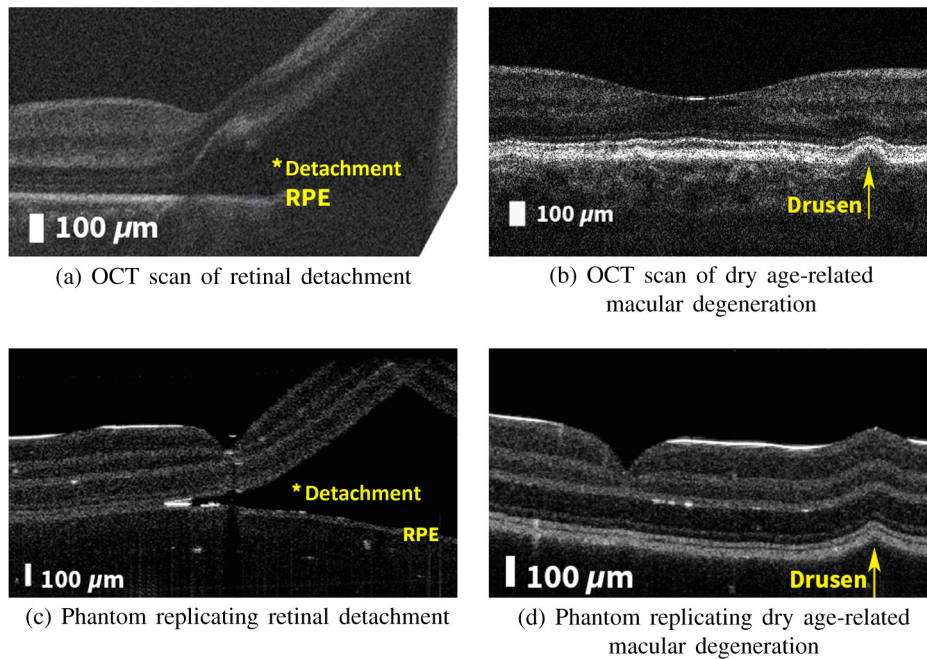


Fig. 8 High resolution OCT B-scans for (a) retinal detachment and (b) dry age-related macular degeneration,²⁵ and the corresponding retinal phantoms replicating the pathologies, (c) retinal detachment and (d) dry age-related macular degeneration.

detachment,¹ the edge of the bump was positioned to be aligned with the foveal pit.

The dry AMD phantom attempts to mimic the single druse build-up under the RPE found in the biological image, as annotated by the arrow in Fig. 8(d). In contrast to the phantom for retinal detachment, the phantom for dry AMD uses a small protrusion of low-scattering PDMS, which is fabricated to be part of the choroid. This serves as a good analog to actual drusen build up, as annotated in Fig. 8(b), making the phantom a potentially useful test object for layer segmentation and drusen detection algorithms. However, one limitation with the current fabrication process is that the inclusion of the drusen protrusion induces curvature in the anterior layers, which does not appear in actual biological images. Also, the foveal pit we created for this phantom does not match the size and shape of the foveal pit found in the biological image. As previously described, a larger foveal pit could be obtained by using beads of a different size.

In both phantoms, bright edges may be occasionally seen within the phantom. These correspond to reflections due to the high refractive mismatch between PDMS and trapped air gaps between the separate layers. Unlike the normal retinal phantom above, the irregular surfaces, which were introduced to mimic the morphologies of these disease, resulted in air gaps that could not be removed even under vacuum.

6 Conclusions

We demonstrated a new fabrication procedure that is capable of recreating anatomically relevant features for retinal imaging, namely structures with nonuniform thickness in a silicone-based retinal phantom. Specifically, the retinal phantom we produced includes variable scattering, variable thickness, and morphologically realistic foveal pit tapering of retinal layers. We have also characterized the effects of changing the mold protrusion dimensions on the resulting foveal pit dimensions. This fabrication procedure was then modified to produce the first retinal

phantoms that replicate the diseased states of retinal detachment and dry AMD.

To the best of our knowledge, this work is the first reported result of a retinal phantom with a realistic foveal pit coupled with correct scattering and thickness properties for the 12 layers of the retina (NFL to choroid, visible under OCT). We have also demonstrated the ability to reproduce features of diseased retinal tissue in silicone-based phantoms. The anatomic accuracy of these phantoms make them reliable standardized samples for development, evaluation, and calibration of OCT systems and protocols, both for clinical and research use in ophthalmology as well as for industrial applications. Furthermore, our characterization of the range and variability of foveal pit dimensions demonstrates the consistency that can be achieved through the reproduction of such phantoms.

The topology of the replica mold, which used a silicon wafer as the base, also gave rise to a relatively flat retinal phantom, except at the foveal pit; the final phantom deviates from the biological tissue where the retina is slightly thicker around the foveal pit, giving rise to a surface with a more pronounced curve. Further work could be done to create a more precise replica mold that would induce the foveal pit formation and tapering of layers while also shaping the retinal layers to have a more curved topology.

The technique for induced tapering of layers that we present may potentially be applied to the fabrication of related phantoms that require layers of nonuniform thicknesses. That said, one key limitation of the proposed fabrication procedure is that the achievable dimensions of the foveal pit are dependent on the glass beads used to create the mold. Due to possible imperfections in manufacturing, it is likely that the glass beads used were not perfect spheres, which negatively impacts the achievable accuracy and consistency in measured dimensions. To overcome this, mono-disperse perfect spheres could be used in the future. In the future, we would also like to investigate other techniques

for better fabrication of drusen-like features. We also recognize that the fabrication procedure we present can only be used to mimic a small range of pathologies. In particular, it is a challenge to induce micrometer-sized defects, such as holes and tears, across layers. Further work may be carried out to investigate procedures for reproducing a more complete set of pathologies relating to retinal tissue.

Acknowledgments

Gary Lee was supported by a scholarship from the Agency for Science, Technology and Research, Singapore. Gennifer Smith was supported through an NSF graduate research fellowship. Monica Agrawal was supported by the Electrical Engineering Research Experience for Undergraduates program in Stanford University, which also provided some financial support for this work.

References

- C. A. Puliafito et al., *Optical Coherence Tomography of Ocular Diseases*, SLACK Inc (1996).
- M. R. Hee et al., "Topography of diabetic macular edema with optical coherence tomography," *Ophthalmology* **105**, 360–370 (1998).
- Diabetic Retinopathy Clinical Research Network, "The relationship between OCT-measured central retinal thickness and visual acuity in diabetic macular edema," *Ophthalmology* **114**(3), 525–536 (2007).
- T. J. Wolfensberger and M. Gonvers, "Optical coherence tomography in the evaluation of incomplete visual acuity recovery after macula-off retinal detachments," *Graefes Arch. Clin. Exp. Ophthalmol.* **240**(2), 85–89 (2002).
- R. de Kinkelder et al., "Comparison of retinal nerve fiber layer thickness measurements by spectral-domain optical coherence tomography systems using a phantom eye model," *J. Biophotonics* **6**, 314–20 (2013).
- F. A. Folgar et al., "Lateral and axial measurement differences between spectral-domain optical coherence tomography systems," *J. Biomed. Opt.* **19**, 016014 (2014).
- J. Baxi et al., "Retina-simulating phantom for optical coherence tomography," *J. Biomed. Opt.* **19**, 021106 (2014).
- T. S. Rowe and R. J. Zawadzki, "New developments in eye models with retina tissue phantoms for ophthalmic optical coherence tomography," *Proc. SPIE* **8229**, 822913 (2012).
- A. M. Dubis, J. T. McAllister, and J. Carroll, "Reconstructing foveal pit morphology from optical coherence tomography imaging," *Br. J. Ophthalmol.* **93**, 1223–7 (2009).
- A. Yazdanpanah et al., "Segmentation of intra-retinal layers from optical coherence tomography images using an active contour approach," *IEEE Trans. Med. Imaging* **30**, 484–496 (2011).
- M. K. Garvin et al., "Automated 3-D intraretinal layer segmentation of macular spectral-domain optical coherence tomography images," *IEEE Trans. Med. Imaging* **28**(9), 1436–1447 (2009).
- G. Quellec et al., "Three-dimensional analysis of retinal layer texture: identification of fluid-filled regions in SD-OCT of the macula," *IEEE Trans. Med. Imaging* **29**(6), 1321–1330 (2010).
- G. Gregori et al., "Spectral domain optical coherence tomography imaging of drusen in nonexudative age-related macular degeneration," *Ophthalmology* **118**(7), 1373–1379 (2011).
- D. Cabrera Fernández, H. M. Salinas, and C. A. Puliafito, "Automated detection of retinal layer structures on optical coherence tomography images," *Opt. Express* **13**(25), 10200–10216 (2005).
- P. P. Srinivasan et al., "Fully automated detection of diabetic macular edema and dry age-related macular degeneration from optical coherence tomography images," *Biomed. Opt. Express* **5**, 3568 (2014).
- G. Staurengi et al., "Proposed lexicon for anatomic landmarks in normal posterior segment spectral-domain optical coherence tomography: the IN-OCT consensus," *Ophthalmology* **121**(8), 1572–1578 (2014).
- M. S. Kim et al., "A study of foveal shape in emmetropia and myopia using spectral domain optical coherence tomography," *J. Korean Ophthalmol. Soc.* **55**(6), 833 (2014).
- T. K. Shih et al., "Fabrication of PDMS (polydimethylsiloxane) microlens and diffuser using replica molding," *Microelectron. Eng.* **83**(11–12), 2499–2503 (2006).
- T. K. Shin, J. R. Ho, and J. W. J. Cheng, "A new approach to polymeric microlens array fabrication using soft replica molding," *IEEE Photonics Technol. Lett.* **16**(9), 2078–2080 (2004).
- A. Bubendorfer, X. Liu, and A. V. Ellis, "Microfabrication of PDMS microchannels using SU-8/PMMA moldings and their sealing to polystyrene substrates," *Smart Mater. Struct.* **16**(2), 367 (2007).
- S. Bhattacharya et al., "Studies on surface wettability of poly(dimethyl) siloxane (PDMS) and glass under oxygen-plasma treatment and correlation with bond strength," *J. Microelectromech. Syst.* **14**, 590–597 (2005).
- D. K. Sardar et al., "Optical scattering, absorption, and polarization of healthy and neovascularized human retinal tissues," *J. Biomed. Opt.* **10**(5), 051501 (2005).
- G. J. Greening et al., "Characterization of thin poly(dimethylsiloxane)-based tissue-simulating phantoms with tunable reduced scattering and absorption coefficients at visible and near-infrared wavelengths," *J. Biomed. Opt.* **19**, 115002 (2014).
- W. Zhang, G. Ferguson, and S. Tatic-Lucic, "Elastomer-supported cold welding for room temperature wafer-level bonding," in *17th IEEE Int. Conf. on Micro Electro Mechanical Systems. Maastricht MEMS 2004 Technical Digest*, pp. 741–744, IEEE (2004).
- S. Farsiu et al., "Quantitative classification of eyes with and without intermediate age-related macular degeneration using optical coherence tomography," *Ophthalmology* **121**, 162–172 (2014).

Gary C. F. Lee is currently an undergraduate student at Stanford University. He is pursuing his BS degree in electrical engineering.

Gennifer T. Smith received her dual-major BS degree in electrical engineering and biology from the University of New Mexico in 2012. Currently, she is a PhD student in electrical engineering at Stanford University.

Monica Agrawal is currently an undergraduate student at Stanford University. She plans to receive a BS degree in electrical engineering and/or computer science.

Theodore Leng is a clinical assistant professor of ophthalmology at the Stanford University School of Medicine. He received an AB/BS and MS degree from Stanford University and his MD degree from Stanford University School of Medicine. After residency training at Bascom Palmer Eye Institute, he completed a postdoctoral fellowship in vitreoretinal diseases and surgery at Stanford. His research interests include imaging informatics, predictive models for disease progression, and serving as the principal investigator of several clinical trials in ophthalmology.

Audrey K. Ellerbee is an assistant professor of electrical engineering at Stanford University. She received her BSE degree from Princeton University, her PhD in biomedical engineering from Duke University, and completed her postdoctoral training in chemistry and chemical biology at Harvard University. Her research interests include applications of optics to medicine and biology. In particular, her research focuses on development of translational imaging technologies, such as optical coherence tomography, for use in the clinic or point-of-care settings.